

# An Ultra-low-loss Compact Phase-Change Material-based Hybrid-mode Interferometer for Photonic Memories

Ranjeet Dwivedi,<sup>1</sup> Fabio Pavanello,<sup>2</sup> and Regis Orobttchouk<sup>1</sup>

<sup>1</sup>*Ecole Centrale de Lyon, CNRS, INSA Lyon, Université Claude Bernard Lyon 1, CPE Lyon, INL, UMR5270, 69130 Ecully, France*

<sup>2</sup>*Univ. Grenoble Alpes, Univ. Savoie Mont Blanc, CNRS, Grenoble INP, CROMA, 38000 Grenoble, France*

(\*Electronic mail: ranjeetdwivedi2@gmail.com)

(Dated: 25 March 2025)

We propose a novel hybrid mode interferometer (HMI) leveraging the interference of hybridized TE-TM modes in a silicon-on-insulator (SOI) waveguide integrated with a GeSe phase change material (PCM) layer. The SOI waveguide's dimensions are optimized to support the hybridization of the fundamental transverse magnetic ( $TM_0$ ) and the first higher transverse electric ( $TE_1$ ) mode. This design allows for efficient and nearly equal power coupling between these two modes, resulting in high-contrast interference when starting from the amorphous PCM state. The PCM's phase transition induces a differential change in the modal effective index, enabling high-contrast transmittance modulation. Our numerical simulations demonstrate a multilevel transmission with a high contrast of nearly 14 dB when the amorphous region's length is varied incrementally, enabling multi-bit storage. The transmittance is maximized in the fully crystalline state with an insertion loss below 0.1 dB. The HMI can also operate as a quasi-pure phase shifter when partially amorphized, making it suitable for Mach-Zehnder interferometers. These characteristics make the proposed device a promising candidate for applications in photonic memories and neuromorphic computing.

Integrated photonic memories are emerging as a promising technology for energy-efficient and high-speed data storage, with potential applications as building blocks in neuromorphic computing<sup>1-6</sup>. Memories based on a thin layer of phase-change material (PCM) placed above a silicon-on-insulator (SOI) waveguide, in contact or in close proximity, are regarded as one of the most promising approaches for next-generation photonic systems. Among the various optical PCMs, GeSbTe (GST) is the most widely studied due to its high refractive index contrast between amorphous and crystalline phases at 1550 nm wavelength. It enables compact device designs utilizing absorption modulation in various configurations<sup>1-4,7</sup>. PCMs have been extensively utilized in Mach-Zehnder interferometers (MZIs), directional couplers, ring resonators, slot waveguides, etc., for, modulation, switching, mode conversion, and other reconfigurable photonic devices<sup>7-17</sup>. Specifically, MZIs require low-loss PCM-based phase shifters to achieve efficient phase modulation with minimal amplitude variation, translating into high extinction ratios. In particular, GST has been extensively explored utilizing incoherent architectures leveraging wavelength division multiplexing for neuromorphic applications<sup>2,4,18</sup>. However, its inherent high absorption limits its applicability in MZI-based coherent photonic circuits, which require low-loss phase shifters<sup>6,19</sup>. Low-loss PCMs integrated on SOI waveguides can offer a nearly pure phase shift<sup>20-23</sup>, with minimal losses due to material absorption and mode field mismatch at the interface of the PCM patch. However, to obtain multilevel transmission, such structures need to be integrated into MZIs, directional couplers, or ring resonators, which increases their overall footprint.

In this paper, we propose a novel compact design based on a SOI waveguide integrated with GeSe, a low-loss PCM. This structure serves dual functions as both a quasi-pure phase modulator and an amplitude modulator, achieved by vary-

ing the crystallization fraction of the GeSe layer. In addition to offering a compact memory, it can serve as a phase shifter in neuromorphic coherent photonic circuits<sup>24</sup>, a memory cell in a photonic tensor core based on a crossbar array<sup>25</sup>, and photonic-electronic dot-product engine for in-memory computing<sup>26</sup>. Our approach leverages the interference between hybridized  $TM_0 - TE_1$  modes in an SOI waveguide with optimized dimensions, enabling high-contrast amplitude modulation through the GeSe phase change. The proposed hybrid mode interferometer (HMI) demonstrates a high contrast of approximately 14 dB in its transmittance between crystalline and amorphous states, with an insertion loss (IL) below 0.1 dB when the PCM is in a fully crystalline state. A contrast exceeding 83% is achieved across the wavelength range of 1.51  $\mu\text{m}$  - 1.58  $\mu\text{m}$ , with a maximum IL in the crystalline state of 0.46 dB. Our calculations indicate that the HMI can achieve multilevel transmittance, allowing for multiple bits of memory. Additionally, the performance of an MZI incorporating HMI in its arms is numerically evaluated, showing multilevel transmission and switching with an IL of approximately 0.7 dB. The results are also compared with those of an HMI and MZI using GST as a PCM. The proposed cross-section can be readily adapted in a CMOS-compatible silicon photonics platform<sup>27</sup>.

Figure 1 illustrates the schematic of the considered hybrid mode interferometric structure, which consists of a waveguide with 50-nm-thick GeSe PCM integrated on top of a standard strip SOI interconnected between identical tapered input/output SOI waveguides. The silicon and buried oxide (BOX) layers have thicknesses of 0.22  $\mu\text{m}$  and 2.0  $\mu\text{m}$ , respectively. The structure is considered to be surrounded by silica in the cladding region. The width of the tapered section is considered to vary between  $w_1$  and  $w_2$  across its length  $L_1$ . The middle section has a uniform width  $w_2$  across its length  $L_2$ . The width of the PCM layer is kept fixed at 1.0  $\mu\text{m}$ . The

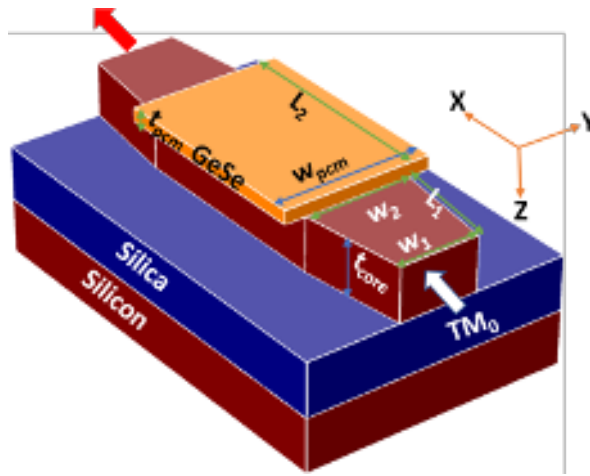


FIG. 1. Schematic of the proposed hybrid mode interferometer.

core dimensions of the input and output ends are selected to support a single TE/TM mode. The dimensions of the middle waveguide are optimized to support hybridized TE-TM modes. We employed the finite difference method using Lumerical Mode solver to calculate the effective indices and polarization fractions. The cross-section of the simulation domain is set to  $4 \mu\text{m} \times 4 \mu\text{m}$ . A Metallic boundary condition is applied, with the center of the silicon core aligned with the center of the simulation region. A non-uniform mesh is employed to optimize accuracy and computational efficiency. A fine mesh of 5 nm is used within a  $2 \mu\text{m} \times 2 \mu\text{m}$  region around the center and a coarser mesh of 10 nm is applied to the outer regions of the simulation domain. The refractive indices of silicon and silica are taken from Palik's data<sup>28</sup>. The refractive index of the PCM layer in its amorphous and crystalline states are taken as  $2.4 + 0.00006i$  and  $2.97 + 0.00006i$ <sup>8</sup>.

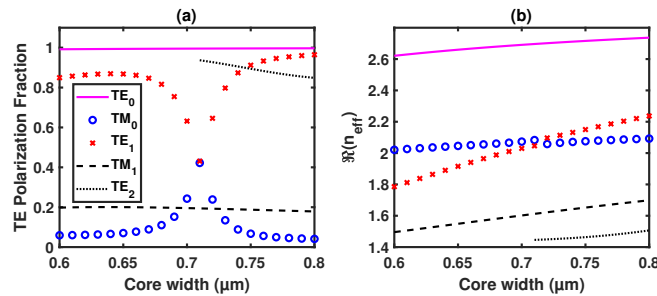
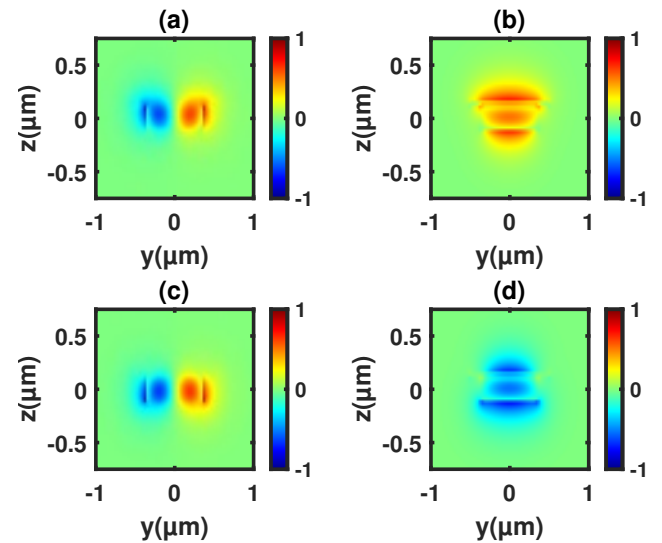


FIG. 2. Variation of (a) TE polarization fraction and (b) real part of the effective index of the different guided modes with the core width for the middle waveguide section. The legend in (a) also applies to (b).

Figure 2(a) shows the variation of the transverse electric (TE) polarization fraction among the various guided TE and TM modes. It should be noted that the TE polarization fraction refers to the proportion of modal power carried by the y-component of the electric field, as the waveguide's cross-section lies in the y-z plane. In our calculations, the wave-

length ( $\lambda$ ) is  $1.55 \mu\text{m}$ , and  $w_2$  is varied in the range of  $0.6 \mu\text{m} - 0.8 \mu\text{m}$ . The PCM layer is considered to be initially in the amorphous state. It can be seen that the TE polarization fraction of the  $TM_0$  ( $TE_1$ ) mode first increases (decreases), reaching a maximum (minimum) at  $w_2 = 0.71 \mu\text{m}$ , and then decreases (increases) after that. At  $w_2 = 0.71 \mu\text{m}$ , the  $TM_0$  and  $TE_1$  modes are hybridized and have nearly equal TE polarization fractions of 42%. The real part of the effective indices of these two modes becomes very close in the hybridization region, as evident in Fig. 2(b). The TE polarization fraction of the  $TE_0$  and  $TE_2$  modes, respectively, remain above 99% and 84% while that for the  $TM_1$  varies between 17% to 20%.

At  $w_2 = 0.71 \mu\text{m}$ , the y and z components of electric fields (denoted by  $E_y$  and  $E_z$ ) of the  $TM_0$ - $TE_1$  hybrid modes, are shown in Fig. 3. The fields are normalized by the maximum electric field across both modes and all field components. This demonstrates that the  $E_y/E_z$  of both modes displays nearly similar patterns while the  $E_z$  of one mode, when inverted with respect to the z-axis, resembles  $-E_z$  of the other hybrid mode.

FIG. 3. Spatial distribution of the  $E_y$  and  $E_z$  electric field components, respectively, for  $TM_0$ - $TE_1$  hybrid mode 1 (a, b) and mode 2 (c, d).

Previous works have utilized hybrid modes in SOI waveguides to design mode converters (e.g., from  $TM_0$  to  $TE_1$  and  $TE_3$ ) using adiabatic long tapered structures<sup>29,30</sup>. However, these designs neither incorporate PCMs nor leverage interference between hybridized modes. In this work, we introduce a PCM layer in the SOI waveguide to create vertical asymmetry, enabling hybridization between the fundamental TM mode and the first higher-order TE mode for optimized core dimensions. The tapered waveguide sections, without supporting mode hybridization, efficiently couple and decouple power between the fundamental TM mode and the hybridized modes. Our structure is designed to achieve high transmittance and low insertion loss in the crystalline state due to constructive interference between the hybridized modes. In con-

trast, when the PCM is fully amorphous, the amplitudes of the hybridized modes become nearly equal, and the phase difference approaches destructive interference, resulting in very low transmittance. By adjusting the amorphous fraction of the PCM, we can control both the phase difference and amplitude of the hybridized modes, enabling multi-bit information encoding through the device's transmittance. To calculate the transmittance of the structure, a TM-polarized input light is considered to excite the fundamental TM mode in the input taper. After propagating to the central waveguide section, light is coupled to the hybridized TE-TM modes. A fraction of the power coupled to the hybridized modes is then back-coupled to the fundamental TM mode at the output end of the last taper, contributing to the output power.

In our calculations, we have taken  $w_1 = 0.4 \mu\text{m}$ ,  $w_2 = 0.71 \mu\text{m}$ , and  $L_1 = 10 \mu\text{m}$  for the tapered section to ensure efficient power coupling between the hybridized modes. Mode overlap calculations show that the power is efficiently coupled to the forward-propagating hybridized modes, leading to negligible reflection at the interfaces. In such a case, the transmittance can be approximated with the interference between these two modes. Therefore, the transmittance can be written as:

$$T \approx |C_1 e^{i\beta_1 L_2} + C_2 e^{i\beta_2 L_2}|^2 \quad (1)$$

Here,  $|C_1|$  ( $|C_2|$ ) represents the magnitude of the product of the modal overlaps between the hybridized  $TM_0 - TE_1$  modes of the central section of the HMI with the fundamental TM mode of the taper at the input and output interfaces. This corresponds to the fraction of power coupled to (from) the  $TM_0 - TE_1$  hybrid modes having propagation constants  $\beta_1$  and  $\beta_2$  from (to) the input (output) taper. The transmittance calculated from Eq. (1) closely matches the results from the eigenmode expansion method, with an error ranging between 0.05% and 2.8% across the wavelength range  $1.45 \mu\text{m} - 1.65 \mu\text{m}$ .

We employed the eigenmode expansion method-based software Lumerical EME to calculate the transmittance of the proposed device. In our calculations, the tapered input and output waveguides are divided into 10 subcells, and the continuously varying cross-sectional subcell (CVCS) method is used. While input is the fundamental TM mode, all the guided modes are considered in each waveguide section. The size of the simulation domain, boundary conditions, and the mesh size in the waveguide cross-section remain the same as discussed previously in the mode calculations. The calculated transmittance is shown in Fig. 4(a) for both amorphous and crystalline phases. It can be seen that the transmittance has a nearly periodic variation with  $L_2$  in both states, which is a result of the interference between the hybrid modes. The transmittance contrast in the amorphous case is  $\approx 1$  due to nearly equal power coupling to the hybrid modes from the tapered section. In the crystalline phase, the polarization fraction of these modes is different, resulting in unequal power coupling and a decrease in contrast. Moreover, the period is different in both states due to different changes in the effective indices of the two modes, leading to a change in the phase difference. Figure 4(b) shows the variation of transmittance contrast between the crystalline and amorphous states and the IL in the

crystalline state. It is found that the contrast is maximum at  $L_2 = 21.1 \mu\text{m}$ , where the transmittance in the amorphous state ( $T_a$ ) is minimum. The IL, however, is minimum at  $L_2 = 25.1 \mu\text{m}$ , where the transmittance in the crystalline state ( $T_c$ ) is maximum. The maxima of the transmittance contrast and the minima of the IL can coincide if the PCM section length is chosen such that the transmittance minimum in the amorphous state aligns with the transmittance maximum in the crystalline state of the PCM. This alignment occurs when the phase difference between the hybridized modes in the amorphous state and the phase difference change after the PCM material undergoes its phase transition is an odd integer multiple of  $\pi$ . In our case, this corresponds to PCM section lengths of  $401.8 \mu\text{m}$  and  $527.7 \mu\text{m}$ , at which we observe insertion losses of 0.007 dB and 0.002 dB, along with transmittance contrasts of 20 dB and 25.7 dB, respectively. To make the device more compact while maintaining reasonable performance, we have explored a relatively shorter length in the design space. For  $L_2$  varying between  $21.1 \mu\text{m}$  and  $25.1 \mu\text{m}$ , the contrast ranges from 36 dB to 10.6 dB, while the IL varies between 0.68 dB and 0.014 dB. Therefore, depending on the requirement, we can select either very high contrast with increased IL or somewhat lower contrast with decreased IL. Given this, we take  $L_2 = 23.7 \mu\text{m}$ , where the contrast is  $\approx 14$  dB and the IL is below 0.1 dB. For this length, the phase difference between the two hybridized modes in the amorphous state is  $1.12\pi$ , which increases by  $0.76\pi$  when the PCM layer transitions to its crystalline state. For a  $\pm 100$  nm change in the PCM section length, the contrast varies by  $-0.3$  dB/ $+0.3$  dB, and the insertion loss changes by  $-0.01$  dB/ $+0.01$  dB. This shows that the imperfect interference does not have a significant impact on the performance of the proposed device.

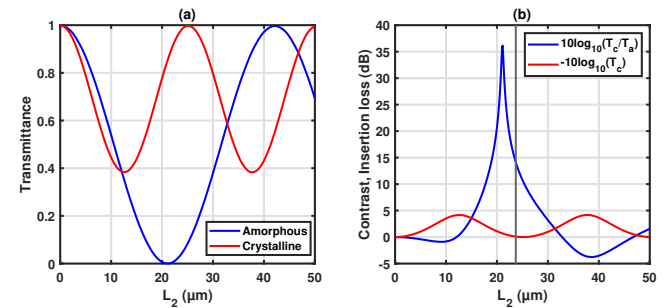


FIG. 4. Variation of (a) transmittance in amorphous (solid blue) and crystalline (dashed red) states, and (b) contrast (solid blue) and insertion loss (dashed red) with the HMI length.

The electric field distribution in the x-y plane passing through the center of the core is shown in Fig. 5, clearly representing the high and low transmittance in the crystalline and amorphous states, respectively.

Next, we calculated the spectral dependence of the proposed HMI. However, due to the lack of an exact dispersion model for the specific data used in our manuscript, we have not included the material dispersion of GeSe. Nonetheless, given the highly compact length of our device, the minor dispersion effects are expected to have very little influence on the



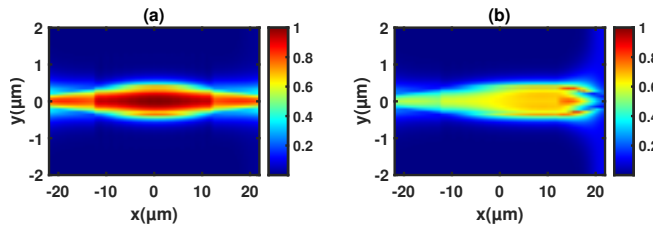


FIG. 5. Spatial map of the electric field magnitude in the x-y plane passing through the center of the waveguide's core in (a) crystalline and (b) amorphous states, respectively.

spectral dependence of the calculated transmittance. Figure 6 presents the transmittance spectra of the HMI in both crystalline and amorphous phases along with the transmittance contrast ( $T_c - T_a$ ). The variation in transmittance is governed by the spectral dependence of the amplitudes and the phase difference between the two hybridized modes. In the crystalline phase, the HMI exhibits a transmittance peak around  $\lambda = 1.58 \mu\text{m}$ , where the condition for constructive interference between the two hybrid modes is closely achieved. The decrease in transmittance by moving away from  $\lambda = 1.58 \mu\text{m}$  corresponds to deviations from the constructive interference condition. In the amorphous state, a transmittance minimum equal to 0.033 is observed at  $\lambda = 1.54 \mu\text{m}$ , where the conditions for destructive interference and equal power coupling between the two modes are closely satisfied. The increase in transmittance in this case is associated with deviations from the destructive interference condition and increasing difference in power coupling between the hybridized modes from the input taper. The maximum contrast is found to be 0.94 with an IL of 0.09 dB (for crystalline GeSe) at  $\lambda = 1.55 \mu\text{m}$ . In the wavelength range of  $1.51 \mu\text{m}$  to  $1.58 \mu\text{m}$ , the HMI demonstrates a contrast of over 83% and a worst-case IL of 0.46 dB. We also present a comparison of the transmittance

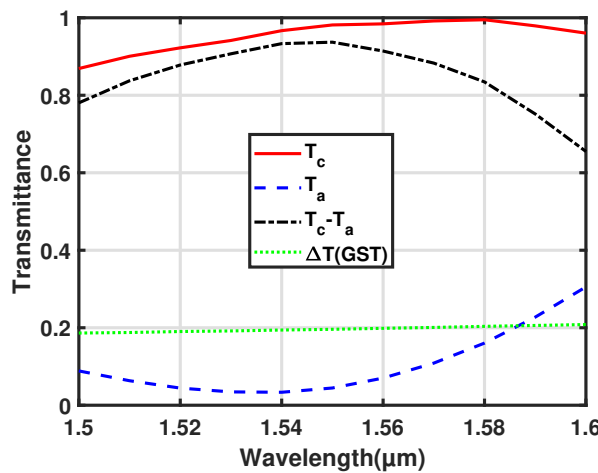


FIG. 6. Spectral variation of transmittance of HMI in crystalline (solid red) and amorphous (dashed blue) state of GeSe. The transmittance contrast is also shown on the same graph for the GeSe (dash-dotted black) and GST (dotted green).

contrast of an HMI incorporating GST as the PCM. The refractive index data of GST in the crystalline and amorphous states are taken as  $6.11 + 0.83i$  and  $3.94 + 0.045i$ <sup>7</sup>. In this case, the thickness of the GST layer is fixed at 20 nm, resulting in an optimum width  $w_2 = 0.69 \mu\text{m}$  that supports mode hybridization in the amorphous state. The length  $L_2$  is taken to be  $40 \mu\text{m}$  to achieve a maximum near the constructive interference regime at  $\lambda = 1.55 \mu\text{m}$ . Notably, due to the significant propagation loss related to the much higher losses in GST, the maximum is not solely dependent on the accumulated phase difference but also on the amplitudes of the modes. For the considered length, the transmittance in the crystalline state of GST is negligible, leading to a transmittance contrast ( $\Delta T$ ) equal to the transmittance in the amorphous state. It should be noted that  $\Delta T$  varies between 0.186 and 0.208, which is significantly lower than the contrast in the case of HMI with GeSe within the considered wavelength range. The slight increase in contrast on the higher wavelength side is attributed to the decrease in modal propagation loss.

We further compared the performance of the proposed HMI device using different low-loss materials. Table I shows the values of refractive indices of different low-loss phase change materials in their crystalline and amorphous states and compares the performance of the proposed HMI using GeSe with other low-loss materials such as  $\text{Sb}_2\text{S}_3$  and  $\text{Sb}_2\text{Se}_3$ . For each material, the core width and PCM thickness were optimized to achieve a nearly equal TE polarization fraction. The length of the PCM section was then adjusted to ensure a transmittance contrast exceeding 14 dB and an insertion loss below 0.1 dB. Despite the higher refractive index contrast between the crystalline and amorphous states in  $\text{Sb}_2\text{S}_3$  and  $\text{Sb}_2\text{Se}_3$ , GeSe outperforms both materials, achieving nearly similar transmittance contrast and insertion loss with a significantly shorter device length. Specifically, the required length for  $\text{Sb}_2\text{S}_3$  is more than twice that of GeSe, while  $\text{Sb}_2\text{Se}_3$  demands nearly an order of magnitude longer PCM section. This difference arises from how the hybridized modes interact with the PCM layer. Although their TE polarization fractions are nearly identical, the hybridized modes interact differently with the PCM layer. Therefore, the PCM layer refractive index and the index contrast between the crystalline and amorphous states highly affect the phase difference between the hybridized modes in the amorphous state and the change in phase difference after the phase transition of the PCM layer. These interactions ultimately influence the device's efficiency and compactness.

After establishing a high-contrast optical transmission between the crystalline and amorphous states of the GeSe PCM, we next explore the potential of the HMI for multilevel photonic memory. For this purpose, we considered the PCM layer to be divided into multiple identical cells, which can change their phase from crystalline to amorphous in an incremental manner. In our calculations, we have considered the PCM layer to be divided into 237 cells, each having 100 nm length. The transmittance in this case is calculated using the Lumerical EME solver and is shown in Fig. 7(a). The PCM layer is initially considered to be in a fully crystalline state, leading to a maximum transmittance of 0.978 (-0.09 dB). The grad-

TABLE I. A comparison of the performance of the proposed HMI using different low loss PCMs such as GeSe, Sb<sub>2</sub>S<sub>3</sub> and Sb<sub>2</sub>Se<sub>3</sub> at  $\lambda = 1.55$   $\mu\text{m}$ . The optimized waveguide dimensions required to achieve nearly equal TE polarization fraction for the hybridized modes are also included. The length required to achieve nearly similar transmittance contrast and insertion loss is compared.

Material	Refractive index Crystalline	Refractive index Amorphous	$w_2(\text{nm})$	$t_{\text{PCM}}(\text{nm})$	TE Polarization fraction	$L_2(\mu\text{m})$	$T_c - T_a(\text{dB})$	IL(dB)
GeSe	$2.97 + 0.00006i^8$	$2.4 + 0.00006i^8$	710	50	0.42, 0.42	23.7	14.1	0.09
Sb <sub>2</sub> S <sub>3</sub>	$3.308 + 0i^{20}$	$2.712 + 0i^{20}$	720	48	0.43, 0.44	55.2	14.2	0.07
Sb <sub>2</sub> Se <sub>3</sub>	$4.050 + 0i^{20}$	$3.285 + 0i^{20}$	740	50	0.42, 0.47	229.2	15.8	0.09

ual switching, e.g., by using local microheaters, of the PCM cells from their initial crystalline state increases the amorphous region across the length of the PCM layer, resulting in a decrease in transmittance. The transmittance scales almost linearly in the range 83.5 % to 21.5 % for the amorphous length in the range 6.6  $\mu\text{m}$  - 15.4  $\mu\text{m}$  (marked by solid red line obtained from linear fitting of data in the range 6.6  $\mu\text{m}$  - 15.4  $\mu\text{m}$ ). A transmittance minimum of 0.038 (-14.2 dB) is achieved when the PCM is fully amorphous, leading to a contrast of  $\approx 14$  dB. The power of the propagating beam during amplitude modulation is predominantly diffracted after exiting the PCM section. This is due to the negligible absorption in the GeSe layer, attributed to its very low imaginary part of the refractive index, and negligible reflection loss at the PCM interface, achieved through the use of tapered waveguides. The modal propagation losses for the hybridized modes are  $4.1 \times 10^{-4}$  dB/ $\mu\text{m}$  and  $3.3 \times 10^{-4}$  dB/ $\mu\text{m}$  in the crystalline state, and  $3.5 \times 10^{-4}$  dB/ $\mu\text{m}$  and  $2.9 \times 10^{-4}$  dB/ $\mu\text{m}$  in the amorphous state. Consequently, the power absorbed in the GeSe layer is estimated to be less than 0.2  $\mu\text{W}/\mu\text{m}$  for an input power of 1 mW. Therefore, the absorption in the GeSe layer is insufficient to induce a phase change or trigger thermo-optic effects. Figure 7(b) shows the variation of the phase of the transmission coefficient with the length of the amorphous region. Interestingly, an amorphized region of only 7.1  $\mu\text{m}$  leads to nearly  $\pi$  phase difference compared to the fully crystalline state. This indicates that an HMI with partial amorphization could be incorporated into the arms of an MZI.

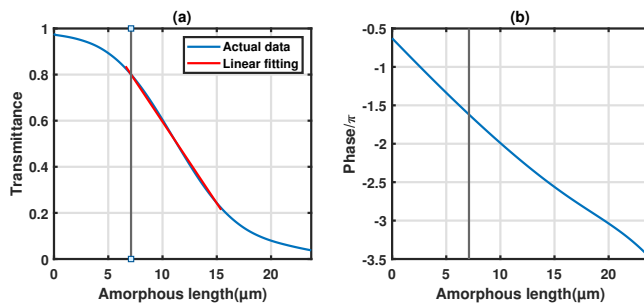


FIG. 7. Variation of (a) transmittance and (b) phase of the transmission coefficient with the length of the amorphous region.

Table II compares the performance of photonic memory devices using various configurations, including straight waveguides (SWG), directional couplers (DC), ring resonators (RR), and multimode interferometers (MMI), with our proposed

HMI design. Notably, our design offers a significantly more compact alternative with a comparable extinction ratio (ER) and IL among devices employing low-loss PCMs.

Finally, we explored the transmission characteristics of an MZI using HMIs in its arms, as shown in Fig. 8. Light (TM polarized) is considered to be launched only in the first input port exciting the  $TM_0$  mode. In our calculations, the IL of the couplers is taken as 0.1 dB. One of the MZI arms is fixed in the crystalline state, while the length of the amorphous region is varied in the other arm. The transmittance at both output ports of the MZI is shown in Fig. 9(a). It can be seen that, with the change in the amorphous/crystalline fraction, the transmittance can be modulated. As expected, a 7.1  $\mu\text{m}$  long amorphous region leads to a power switching between the two output ports due to the  $\pi$  phase difference between the two arms. The highest IL is found to be  $\sim 0.7$  dB. For comparison, the transmittance of an MZI incorporating GST in its arms is shown in Fig. 9 (b). The injection mode at the first input port of the MZI is again a  $TM_0$  mode. However, unlike the GeSe-based MZI, we did not utilize a GST-based HMI structure in the MZI arms. Instead, we employed a SOI waveguide integrated with a 20 nm thick, 3  $\mu\text{m}$  long GST patch to achieve lower IL. The width of the SOI waveguide and that of GST is taken as 400 nm. For the considered dimensions of the GST, nearly  $\pi$  phase difference is obtained between the transmission coefficients of the crystalline and amorphous states. It can be seen that the transmittance at both ports is very low when both arms are in a fully crystalline state. With the increase in the length of the amorphous region, the total transmittance is increased, reaching a maximum of around 45% when the GST layer in one of the arms becomes fully amorphous. The IL in this case is found to vary between 15 dB and 3.5 dB due to the imbalance created by the high absorption loss of GST.

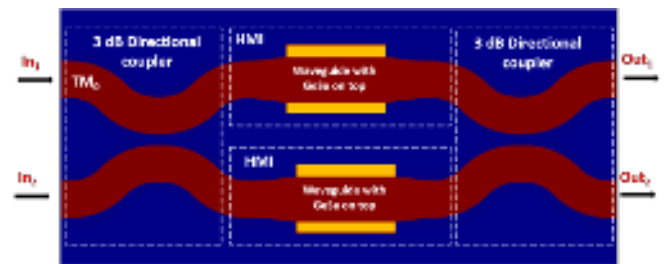


FIG. 8. 2x2 MZI configuration with 3 dB directional couplers and HMI in each arm.

TABLE II. A comparison of the performance of the proposed HMI with other phase change memory devices.

Waveguide structure	Configuration	Programming	Multilevel Transmission	Footprint	ER	IL(dB)
Sb <sub>2</sub> Se <sub>3</sub> on Si waveguide <sup>21</sup>	DC	Electrical	Arbitrary	33 $\mu\text{m}$ long excluding bends	15 dB	0.36
Sb <sub>2</sub> Se <sub>3</sub> on Si waveguide <sup>10</sup>	RR	Electrical	5 bit	30 $\mu\text{m}$ radius	>10 dB	<1
Sb <sub>2</sub> Se <sub>3</sub> , Sb <sub>2</sub> S <sub>3</sub> on Si waveguide <sup>22</sup>	DC	Electrical	2bit	25 $\mu\text{m}$ and 67 $\mu\text{m}$ long excluding bends	20 dB	<0.1
Sb <sub>2</sub> Se <sub>3</sub> on Si waveguide <sup>31</sup>	MMI	None	1 bit	27 $\mu\text{m}$ long excluding bends	>15 dB	$\sim 1$
Ge <sub>2</sub> Sb <sub>2</sub> Se <sub>5</sub> on Si waveguide <sup>32</sup>	SWG	Electrical	4 bit	80 $\mu\text{m}$ long	$\sim 12$ dB	$\sim 0.12$
N-doped GST on Si waveguide <sup>4</sup>	SWG	Electrical	7 bit	2.5 $\mu\text{m}$ long	>20 dB	$\sim 1$
Segmented GST on Si waveguide <sup>17</sup>	SWG	Electrical	6 bit	10 $\mu\text{m}$ long	$\sim 10$ dB	$\sim 1.5$
GST on Si <sub>3</sub> N <sub>4</sub> waveguide <sup>33</sup>	SWG	Optical	5 bit	2 $\mu\text{m}$ long	$\sim 30\%$	-
GeSe on Si waveguide*	HMI	Simulation	Multi bit	24 $\mu\text{m}$ long	$\sim 14$ dB	<0.1

\*Present work

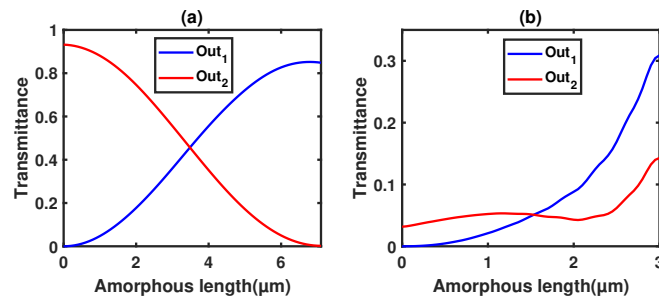
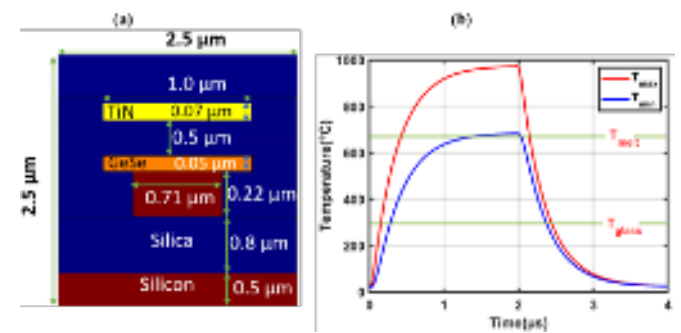


FIG. 9. Variation in transmittance of an MZI with (a) HMI and (b) GST-based arms, as a function of increasing amorphous region in one of the arms.

Therefore, it is clear that using GST in an MZI configuration suffers from high IL and low contrast compared to GeSe-based approaches. The IL of a GeSe-based MZI can be further minimized by employing a simple GeSe-based phase shifter without an HMI. For instance, a GeSe patch with a thickness of 50 nm and a width of 400 nm integrated on an SOI waveguide with the same width and a thickness of 220 nm can achieve a  $\pi$  phase shift between the crystalline and amorphous states over a patch length of 8  $\mu\text{m}$ . When this phase shifter is incorporated into the MZI arms, it enables power switching between the output ports, with an IL of 0.54 dB compared to 0.7 dB in the HMI-based MZI configuration. It is important to note that the IL in the HMI-based MZI arms is primarily due to slight amplitude variations in the transmittance during phase shifts. On the other hand, the IL in simple GeSe patch-based MZI arms is mainly caused by mode field mismatches at the GeSe interfaces. The proposed HMI device has a compact footprint of approximately 44  $\mu\text{m}^2$ , making it considerably smaller than a standard  $1 \times 1$  MZI, which incorporates  $1 \times 2$  power splitters at both the input and output, each occupying over 50  $\mu\text{m}^2$  space<sup>34</sup>. These memories can be written either optically, using in-plane or out-of-plane optical pulses, or electrically, via integrated heaters.

We numerically investigate the phase-change behavior of the GeSe PCM layer. For this purpose, we consider an integrated titanium nitride (TiN) heater layer positioned above the GeSe layer. The schematic of 2D simulation geometry is illus-

FIG. 10. (a) Schematic of the considered geometry for thermal simulations and (b) temporal variation of maximum and minimum temperatures ( $T_{max}$  and  $T_{min}$ ) across GeSe.

trated in Fig. 10(a), with the simulation domain extending 2.5  $\mu\text{m}$  in both width and thickness. In our thermal simulations, the substrate, BOX, cladding, and heater layer thicknesses are set to 0.5  $\mu\text{m}$ , 0.8  $\mu\text{m}$ , 1.2  $\mu\text{m}$ , and 0.07  $\mu\text{m}$ , respectively. To minimize any influence on optical transmission characteristics, the heater is separated from the GeSe layer by 0.5  $\mu\text{m}$ . The heater width is chosen to match the width of the GeSe layer to ensure uniform thermal distribution. Transient thermal simulations are carried out using Lumerical HEAT software. The simulation domain boundaries and the initial temperature are set to room temperature (22  $^{\circ}\text{C}$ ). The heater is considered to dissipate a power of 12.5 mW/ $\mu\text{m}$  for a duration of 2  $\mu\text{s}$ . The thermal properties of the materials used in simulations are summarized in Table III. Due to spatially nonuniform heating within the GeSe layer, we show the variation of maximum and minimum temperatures ( $T_{max}$  and  $T_{min}$ ) across the PCM in Fig. 10(b). The applied heat pulse ensures that both  $T_{max}$  and  $T_{min}$  exceed the melting temperature of GeSe ( $T_{melt} = 670$   $^{\circ}\text{C}$ <sup>37</sup>). After switching off the heater, both temperatures rapidly drop below the glass transition temperature ( $T_{glass} = 295$   $^{\circ}\text{C}$ <sup>38</sup>). The calculated cooling rates from  $T_{melt}$  to  $T_{glass}$  for  $T_{max}$  and  $T_{min}$  are approximately 1.26 K/ns and 1.09 K/ns, respectively. These cooling rates are expected to be sufficiently high to suppress recrystallization during melt quenching, enabling full amorphization of the PCM layer. In the absence of experimentally reported critical quenching



TABLE III. Properties of the different materials used in thermal simulations.

Material	Thermal Conductivity( $W/mK$ )	Heat capacity ( $J/KgK$ )	Density ( $Kg/m^3$ )
TiN	29	388	5210
GeSe	1.5 crystalline <sup>35</sup>	329 <sup>35</sup>	5520 <sup>35</sup>
	1.3 amorphous <sup>36</sup>		
SiO <sub>2</sub>	1.38	709	2203
Si	148	711	2330

rates for GeSe, we have referenced the well-established value for GST ( $> 1$  K/ns)<sup>39</sup>. For recrystallization of the amorphized GeSe, the PCM layer can be heated above  $T_{glass}$  and below  $T_{melt}$  for a sufficiently long duration (ranging from a few microseconds to milliseconds) by applying heat pulses with appropriate power and timing. Our calculations show that recrystallization can be achieved with a heat pulse of 6 mW/ $\mu$ m power applied for 50  $\mu$ s, which maintains the temperature of the entire PCM layer between the crystallization and melting temperatures for around 49  $\mu$ s. More energy-efficient and optimized heater cross-sections can be explored depending on the platform. Furthermore, the heater geometry can be tailored along the propagation direction for gradual phase transitions of the PCM layer depending on the number of intermediate levels desired.

We proposed the design of a novel hybrid mode interferometer exploiting the interference between hybridized  $TM_0 - TE_1$  modes of an SOI waveguide integrated with GeSe PCM. For the optimized dimensions, the HMI shows a high transmission contrast between the crystalline and amorphous states of GeSe. Moreover, a contrast above 83% is obtained in the wavelength range 1.51  $\mu$ m - 1.58  $\mu$ m. The multilevel transmission performance is simulated considering a gradual increase in the length of the amorphous region showing a contrast of  $\approx 14$  dB between fully crystalline and fully amorphous GeSe, with a fully crystalline state IL  $< 0.1$  dB at  $\lambda = 1.55$   $\mu$ m. The HMI can act as a quasi-pure phase shifter with partial amorphization, enabling its integration into MZIs. These features make the HMI memory device a promising candidate for energy-efficient neuromorphic and in-memory photonic computing. The proposed device has quite a small footprint (43.7  $\mu$ m  $\times$  1  $\mu$ m) compared to a standard  $1 \times 1$  MZI.

## ACKNOWLEDGMENTS

This work has received funding from the European Union's Horizon Europe research and innovation program under the grant agreement No. 101070238.

## AUTHOR DECLARATIONS

### Conflict of Interest

The authors have no conflicts to disclose.

## Author Contributions

**Ranjeet Dwivedi:** Conceptualization (equal); Data curation (lead); Formal analysis (equal); Methodology (lead); Software (lead); Visualization (lead); Writing – original draft (lead); Writing – review & editing (equal). **Fabio Pavanello:** Conceptualization (equal); Formal analysis (equal); Funding acquisition (equal); Methodology (supporting); Project Administration (lead); Supervision (equal); Writing – review & editing (equal). **Regis Orobthchouk:** Conceptualization (equal); Formal analysis (equal); Funding acquisition (equal); Methodology (supporting); Supervision (equal); Writing – review & editing (equal).

## DATA AVAILABILITY STATEMENT

The data that support the findings of this study are available from the corresponding author upon reasonable request.

## REFERENCES

- X. Li, N. Youngblood, C. Ríos, Z. Cheng, C. D. Wright, W. H. Pernice, and H. Bhaskaran, "Fast and reliable storage using a 5 bit, nonvolatile photonic memory cell," *Optica* **6**, 1–6 (2019).
- S. G.-C. Carrillo, A. Lugnan, E. Gemo, P. Bienstman, W. H. Pernice, H. Bhaskaran, and C. D. Wright, "System-level simulation for integrated phase-change photonics," *Journal of Lightwave Technology* **39**, 6392–6402 (2021).
- S. G.-C. Carrillo, E. Gemo, X. Li, N. Youngblood, A. Katumba, P. Bienstman, W. Pernice, H. Bhaskaran, and C. D. Wright, "Behavioral modeling of integrated phase-change photonic devices for neuromorphic computing applications," *APL Materials* **7** (2019).
- J. Xia, T. Wang, Z. Wang, J. Gong, Y. Dong, R. Yang, and X. Miao, "Seven bit nonvolatile electrically programmable photonics based on phase-change materials for image recognition," *ACS Photonics* **11**, 723–730 (2024).
- C. Wu, H. Deng, Y.-S. Huang, H. Yu, I. Takeuchi, C. A. Ríos Ocampo, and M. Li, "Freeform direct-write and rewritable photonic integrated circuits in phase-change thin films," *Science Advances* **10**, eadk1361 (2024).
- A. Tsakyridis, M. Moralis-Pegios, G. Giamougiannis, M. Kirtas, N. Paspalis, A. Tefas, and N. Pleros, "Photonic neural networks and optics-informed deep learning fundamentals," *APL Photonics* **9** (2024).
- X. Yan, B. Chen, and Y. Lu, "High optical contrast and multi-level storage of the ultracompact plasmonic device based on phase change materials," *Optics & Laser Technology* **170**, 110239 (2024).
- R. Soref, J. Hendrickson, H. Liang, A. Majumdar, J. Mu, X. Li, and W.-P. Huang, "Electro-optical switching at 1550 nm using a two-state geese phase-change layer," *Optics express* **23**, 1536–1546 (2015).
- N. Dhingra, J. Song, G. J. Saxena, E. K. Sharma, and B. Rahman, "Design of a compact low-loss phase shifter based on optical phase change material," *IEEE Photonics Technology Letters* **31**, 1757–1760 (2019).

This is the author's peer reviewed, accepted manuscript. However, the online version of record will be different from this version once it has been copyedited and typeset.

PLEASE CITE THIS ARTICLE AS DOI: 10.1063/1.50245618

- <sup>10</sup>R. Chen, Z. Fang, C. Perez, F. Miller, K. Kumari, A. Saxena, J. Zheng, S. J. Geiger, K. E. Goodson, and A. Majumdar, "Non-volatile electrically programmable integrated photonics with a 5-bit operation," *Nature Communications* **14**, 3465 (2023).
- <sup>11</sup>R. Chen, V. Tara, M. Choi, J. Dutta, J. Sim, J. Ye, Z. Fang, J. Zheng, and A. Majumdar, "Deterministic quasi-continuous tuning of phase-change material integrated on a high-volume 300-mm silicon photonics platform," *npj Nanophotonics* **1**, 7 (2024).
- <sup>12</sup>R. Soref, F. De Leonardis, M. De Carlo, and V. M. Passaro, "Compact non-volatile multilevel sb2se3 electro-optical switching in the mid-infrared group-iv-photonics platform," *Optics & Laser Technology* **176**, 111005 (2024).
- <sup>13</sup>J. Zhang, J. Zheng, P. Xu, Y. Wang, and A. Majumdar, "Ultra-low-power nonvolatile integrated photonic switches and modulators based on nanogap-enhanced phase-change waveguides," *Optics Express* **28**, 37265–37275 (2020).
- <sup>14</sup>Z. Quan, Y. Wan, X. Ma, and J. Wang, "Nonvolatile multi-level adjustable optical switch based on the phase change material," *Optics Express* **30**, 36096–36109 (2022).
- <sup>15</sup>C. Song, Y. Gao, G. Wang, Y. Chen, P. Xu, C. Gu, Y. Shi, and X. Shen, "Compact nonvolatile  $2 \times 2$  photonic switch based on two-mode interference," *Optics Express* **30**, 30430–30440 (2022).
- <sup>16</sup>M. Wei, X. Lin, K. Xu, Y. Wu, C. Wang, Z. Wang, K. Lei, K. Bao, J. Li, L. Li, *et al.*, "Inverse design of compact nonvolatile reconfigurable silicon photonic devices with phase-change materials," *Nanophotonics* **13**, 2183–2192 (2024).
- <sup>17</sup>C. Zhang, M. Wei, J. Zheng, S. Liu, H. Cao, Y. Huang, Y. Tan, M. Zhang, Y. Xie, Z. Yu, *et al.*, "Nonvolatile multilevel switching of silicon photonic devices with in2o3/gst segmented structures," *Advanced Optical Materials* **11**, 2202748 (2023).
- <sup>18</sup>P. Guo, N. Zhou, W. Hou, and L. Guo, "Starlight: a photonic neural network accelerator featuring a hybrid mode-wavelength division multiplexing and photonic nonvolatile memory," *Optics Express* **30**, 37051–37065 (2022).
- <sup>19</sup>N. C. Harris, J. Carolan, D. Bunandar, M. Prabhu, M. Hochberg, T. Baehr-Jones, M. L. Fanto, A. M. Smith, C. C. Tison, P. M. Alsing, *et al.*, "Linear programmable nanophotonic processors," *Optica* **5**, 1623–1631 (2018).
- <sup>20</sup>M. Delaney, I. Zimpeckis, D. Lawson, D. W. Hewak, and O. L. Muskens, "A new family of ultralow loss reversible phase-change materials for photonic integrated circuits: Sb2s3 and sb2se3," *Advanced functional materials* **30**, 2002447 (2020).
- <sup>21</sup>Z. Fang, B. Mills, R. Chen, J. Zhang, P. Xu, J. Hu, and A. Majumdar, "Arbitrary programming of racetrack resonators using low-loss phase-change material sb2se3," *Nano Letters* **24**, 97–103 (2023).
- <sup>22</sup>T. Y. Teo, M. Krbal, J. Mistrik, J. Prikryl, L. Lu, and R. E. Simpson, "Comparison and analysis of phase change materials-based reconfigurable silicon photonic directional couplers," *Optical Materials Express* **12**, 606–621 (2022).
- <sup>23</sup>J. Zheng, Z. Fang, C. Wu, S. Zhu, P. Xu, J. K. Doylend, S. Deshmukh, E. Pop, S. Dunham, M. Li, *et al.*, "Nonvolatile electrically reconfigurable integrated photonic switch enabled by a silicon pin diode heater," *Advanced Materials* **32**, 2001218 (2020).
- <sup>24</sup>Y. Shen, N. C. Harris, S. Skirlo, M. Prabhu, T. Baehr-Jones, M. Hochberg, X. Sun, S. Zhao, H. Larochelle, D. Englund, *et al.*, "Deep learning with coherent nanophotonic circuits," *Nature photonics* **11**, 441–446 (2017).
- <sup>25</sup>J. Feldmann, N. Youngblood, M. Karpov, H. Gehring, X. Li, M. Stappers, M. Le Gallo, X. Fu, A. Lukashchuk, A. S. Raja, *et al.*, "Parallel convolutional processing using an integrated photonic tensor core," *Nature* **589**, 52–58 (2021).
- <sup>26</sup>W. Zhou, B. Dong, N. Farmakidis, X. Li, N. Youngblood, K. Huang, Y. He, C. David Wright, W. H. Pernice, and H. Bhaskaran, "In-memory photonic dot-product engine with electrically programmable weight banks," *Nature Communications* **14**, 2887 (2023).
- <sup>27</sup>F. Pavanello, C. Marchand, I. O'Connor, R. Orobtcchouk, F. Mandorlo, X. Letartre, S. Cuffe, E. I. Vatajelu, G. Di Natale, B. Cluzel, A. Coillet, B. Charbonnier, P. Noé, F. Kavan, M. Zoldak, M. Szaj, P. Bienstman, T. Van Vaerenbergh, U. Ruhrmair, P. Flores, L. G. e Silva, R. Chaves, L.-M. Silveira, M. Ceccato, D. Gizopoulos, G. Papadimitriou, V. Karakostas, A. Brando, F. J. Cazorla, R. Canal, P. Closas, A. Gusi-Amigó, P. Crovetti, A. Carpegna, T. M. Carmona, S. Di Carlo, and A. Savino, "Neuropuls: Neuromorphic energy-efficient secure accelerators based on phase change materials augmented silicon photonics," in *2023 IEEE European Test Symposium (ETS)* (2023) pp. 1–6.
- <sup>28</sup>E. D. Palik, *Handbook of optical constants of solids*, Vol. 1 (Academic press, 1998).
- <sup>29</sup>D. Dai, Y. Tang, and J. E. Bowers, "Mode conversion in tapered submicron silicon ridge optical waveguides," *Optics express* **20**, 13425–13439 (2012).
- <sup>30</sup>D. Dai and M. Zhang, "Mode hybridization and conversion in silicon-on-insulator nanowires with angled sidewalls," *Optics express* **23**, 32452–32464 (2015).
- <sup>31</sup>K. Shang, L. Niu, H. Jin, H. Wang, W. Zhang, F. Gan, and P. Xu, "Non-volatile  $2 \times 2$  optical switch using multimode interference in an sb2se3-loaded waveguide," *Optics Letters* **49**, 722–725 (2024).
- <sup>32</sup>J. Meng, Y. Gui, B. M. Nouri, X. Ma, Y. Zhang, C.-C. Popescu, M. Kang, M. Miscuglio, N. Peserico, K. Richardson, *et al.*, "Electrical programmable multilevel nonvolatile photonic random-access memory," *Light: Science & Applications* **12**, 189 (2023).
- <sup>33</sup>X. Li, N. Youngblood, C. Ríos, Z. Cheng, C. D. Wright, W. H. Pernice, and H. Bhaskaran, "Fast and reliable storage using a 5 bit, nonvolatile photonic memory cell," *Optica* **6**, 1–6 (2018).
- <sup>34</sup>S. Han, W. Liu, and Y. Shi, "Ultra-broadband dual-polarization power splitter based on silicon subwavelength gratings," *IEEE Photonics Technology Letters* **33**, 765–768 (2021).
- <sup>35</sup>X. Zhang, J. Shen, S. Lin, J. Li, Z. Chen, W. Li, and Y. Pei, "Thermoelectric properties of gese," *Journal of Materiomics* **2**, 331–337 (2016).
- <sup>36</sup>D. Todorović, P. Nikolić, D. Vasiljević, and M. Dramićanin, "Photoacoustic investigation of thermal and transport properties of amorphous gese thin films," *Journal of applied physics* **76**, 4012–4021 (1994).
- <sup>37</sup>H. Wiedemeier and P. Siemers, "The thermal expansion and high temperature transformation of gese," *Zeitschrift für anorganische und allgemeine Chemie* **411**, 90–96 (1975).
- <sup>38</sup>J. Pries, S. Wei, M. Wuttig, and P. Lucas, "Switching between crystallization from the glassy and the undercooled liquid phase in phase change material ge2sb2te5," *Advanced materials* **31**, 1900784 (2019).
- <sup>39</sup>M. Wuttig, H. Bhaskaran, and T. Taubner, "Phase-change materials for non-volatile photonic applications," *Nature photonics* **11**, 465–476 (2017).